

Hybrid Lattice Particle Modeling of Wave Propagation Induced Fracture of Solids

G. Wang^{1,*}, A. Al-Ostaz¹, A.H.-D. Cheng¹, P.R. Mantena²

¹Department of Civil Engineering, University of Mississippi, University, MS 38677

²Department of Mechanical Engineering, University of Mississippi, University, MS 38677

Abstract

This paper presents a discrete dynamic fracture model, hybrid lattice particle modeling (HLPM), and its application in the wave propagation induced fracture problems of solids. The HLPM is established based on a combination of the first author's prior particle modeling (PM) technique with the conventional lattice modeling (LM) theory. The HLPM has the robustness of simulating the dynamic fragmentation of solids under high strain rate loadings at macroscales with a various Poisson ratio extent. In this paper, first, the wave propagation in 1D and 2D homogenous materials with HLPM is modeled and the obtained results are validated by a comparison with the analytical solutions; then, two HLPM simulations of the wave propagation induced fracture, spall cracks, due to impact and blasting, are completed. In the impact case, spall crack formation due to hyper-velocity impact is captured, and the HLPM results are in good agreement with the analogous molecular dynamics (MD) simulations by Krivtsov [1999]. Moreover, a functionally designed infrastructure material coated with a high strength layer, but with different coating strengths at the interface, is also investigated to find out the protective effect of spallation. The modeling results demonstrate that prevention of material from spallation under extreme loadings is difficult; it needs the coating material with super strength. In the blasting study, the fracturing efficiency associated with the spatial explosive setup is investigated. This will benefit the explosive fracturing applications.

Keywords: hybrid lattice particle modeling, dynamic fracture, wave propagation, homogenous materials, spall crack, blast

* Corresponding author: Ge Wang, Email: gewang@olemiss.edu Tel: + 662 915 1975, Fax: + 662 915 5523

1. Introduction

Dynamic fracture and fragmentation under high strain rate loads (impact, blasting, crush, collapse, high speed puncture/penetration, comminution, etc.) has broad civilian/military applications, among which the explosive related applications, seismological studies, shock synthesis and ballistic impacts are currently the most challenging areas to the numerical models. In the above-listed areas, the wave propagation dominates the formation and evolution of the dynamic fracture pattern, and the fragments, e.g., spall cracks, are often induced by the internal wave interactions. Thus, a good model is required not only to be able to correctly predict wave but also the consequent induced fracture.

Static or quasi-static models have existed for several decades and successfully been used for micromechanics and macro-mechanics structure analysis. However, they fail to become a tool for dynamic fracture of solids. The reason arises from the fundamental differences between static (or quasi-static) and dynamic deformation. In quasi-static deformation, at any time, a situation of static equilibrium holds, which implies that any element in the material body has a summation of forces acting on it close to zero. In contrast, in dynamic deformation, when a high strain rate loading is applied to the boundary of the body, the stress propagates, that is, the stress has to travel through the body. This is called wave propagation, usually measured by Hopkinson bar test [1]. Thus, dynamic deformation often involves wave propagation. Consequently, a sequence of states of equilibrium defined by the well-known equations of mechanics of materials (summation of forces equal to zero, summation of moments equal to zero; compatibility of strain; constitutive relations, etc.) are no longer valid. In hyper-velocity impact and blast explorations, wave propagation of solids is the key to understand the resultant fracture and fragments. Moreover, wave propagation study can provide important outcomes for fracture control which has remarkable significance to engineering applications.

Numerically, current continuum mechanics based models (CMBM for short), e.g., finite element method (FEM), can indeed accurately solve the wave propagation of solids even in case of large deformation. However, they limit to fracture/fragmentation. The FEM regards material as one continuum media, and constitutive equations are applied within each element; hence, once the continuity of material is broken due to the occurrence of fracture or fragmentation, new mesh

system is required to generate for the next cycle of computation. When a material body is subject to extreme loadings, unexpected fragments are often produced. Herein, this offers FEM an extreme challenge in technique to deal with the dynamic re-meshing, and causes the computation highly expensive. As such, discrete element based methods (DEBM for short), e.g, smoothed particle hydrodynamics (SPH) [2], particle flow code (PFC) [3] and particle modeling (PM) [4-5], etc., have been established at macroscopic level. DEBM is established based on treating material as an assemblage of mass particles. The constitutive equations are assigned to define the interactions among the discrete neighboring particles. This leads to DEBM unique robustness to solve the 'discontinuity of material' problems. Figure 1 displays the comparison of using FEM and SPH in simulating material penetration [6]. It is seen that although the FEM employs a powerful re-meshing technique, arbitrary Lagrange Euler (ALE), the fragmentation is still not able to be predicted. As such, there are newly developed models that combine CMBM and DEBM, e.g., particle finite element method (PFEM) [7] and material point method (MPM) [8], by which the deformation is solved using CMBM while the fracture/fragmentation relies on DEBM. Due to the irreplaceable superiority of DEBM to CMBM in solving the fragmentation of materials, the 'discrete material' concept is becoming more and more widely accepted by engineering fields, and the market for DEBM applications is increasingly growing. This gives rise to a prosperous DEBM modeling research in this decade.

Hybrid lattice particle modeling (HLPM) is the one among a number of the branches of DEBM [8]. The HLPM has been proposed that combines the strengths of lattice model (LM) [10-11] and PM [4-5], in which the interaction potential can be described by employing either linear (quadratic) or nonlinear (Lennard-Jones or polynomial) type to the axial/angular linkage. The defined spring constants are then mapped into lattice system, which are in turn matched with the material's continuum-level elastic moduli and strength. The HLPM can readily simulate dynamic behaviors of materials at macro-scales with a varying Poisson's ratio extent [9]. The principle of HLPM can be described as follows: the particle-particle interaction is derived from lattice modeling (LM) theory whereas the computational scheme follows particle modeling (PM) technique. Once the translational strength is exceeded, the spring is broken and a fracture is created.

The advantages of HLPM over the existing discrete element based methods can be summarized as follows:

- (1) Easy for the determination of input parameters. Four conservative/equivalent rules (mass, potential energy, Young's modulus and tensile/compression strength) are required to determine the material properties for the input datasheet.
- (2) Easy for implementation and high computation efficiency. Since the physical size of each particle is ignored other than its equivalent mass, the algorithm of coding a HLPM computation is fairly easy; meanwhile, since no computation is spent in keeping track of the instantaneous contact positions and the evolving geometry of all elements, the HLPM computing cost is greatly reduced.

Since its establishment, a successful HLPM simulation have been firstly achieved in predicting the fracture pattern of an epoxy plate with randomly distributed holes in tension [12], in which simulation, the Poisson's ratio of epoxy was set to 1/3. This is a special case of HLPM in which all the angular interactions are absent [9]. Moreover, two successful qualitative comparisons currently have been completed with the dynamic failure experiments of polymeric material (nylon-6,6 and vinyl ester) indentation [13,14], respectively.

After gaining the confidence of HLPM from the above-mentioned fracture study cases, in this paper, we step forward to investigate the modeling capability of the HLPM on the wave propagation induced fracture problems. As the wave propagation in the lattice and the particle model (spring connections) is somewhat different from that of the continuum media, it is not clear that the physical phenomenon of wave propagation can be correctly predicted. Thus, to have confidence in HLPM model for simulating wave dominated problems, it needs to be tested and validated.

In what follows, we first briefly introduce the HLPM algorithm. It is then applied to one- and two-dimensional wave propagation problems. The obtained HLPM results are verified with the analytical solutions. Next, the HLPM is applied to the simulation of wave propagation induced fracture, spall cracks, due to impact and blasting. In the impact case, a functionally designed infrastructure material coated with a high strength layer, but with different coating

strengths at the interface, is also investigated to find out the protective effect of spallation. The ultimate application for HLPM is aimed at shock synthesis.

2. Model Description

The hybrid lattice particle model (HLPM)—also called lattice particle simulation, discrete modeling, or quasi-molecular modeling—is a dynamic simulation model that typically uses a relatively small number of particles of macroscopic sizes, representing solid and/or fluid mass. The particles' location and velocity evolves according to the laws of Newtonian mechanics. The axial force interaction between particles is modeled after Wang and Ostoja-Starzewski [4] (reason: conventional LM only works for linear considerations), which is matched up with the Young's modulus and tensile strength of the material as well as energy and mass. The angular force interaction between the adjacent sides of each particle is after Wang, *et al.* [9]. In principle, the distance of particle spacing can decrease to a few angstroms; in that case we recover a molecular dynamics like model. Hence the HLPM is fairly flexible in modeling physical phenomena of all sizes, limited only by the number of particles needed in the modeling (computational power).

The theoretical derivation of non-thermal-based HLPM can be briefly reviewed as follows.

In HLPM, the non-linear axial interaction force between neighboring (quasi-) particles, F , can alternatively take the same form as in MD:

$$F = -\frac{G}{r^p} + \frac{H}{r^q} \quad (1)$$

Here G , H , p and q are positive constants, and $q > p \geq 1$ to obtain the repulsive effect that is necessarily (much) stronger than the attractive one, r being the distance between two particles.

Ashby & Jones [15] presented a simple method to evaluate continuum-type Young's modulus E and tensile stress $\sigma(r)$ of the material from $F(r)$, namely

$$E = \frac{S_0}{r_0} \quad (2)$$

and

$$\sigma(r) = NF(r) \quad (3)$$

where $S_0 = (dF/dr)_{r=r_0}$, and r_0 is the equilibrium spacing between contiguous particles. N is the number of bonds/unit area, equal to $1/r_0^2$. Tensile strength, σ_{TS} , results when $dF(r_d)/dr = 0$, that yields,

$$\sigma_{TS} = NF(r_d) \quad (4)$$

Note that Eq. (2) has been demonstrated to be completely consistent with LM derivation [8].

Just as in MD, the non-linear dynamical equation of motion for each particle P_i of the PM system is given by

$$m_i \frac{d^2 \vec{r}_i}{dt^2} = \sum \left[\left(-\frac{G_i}{r_{ij}^p} + \frac{H_i}{r_{ij}^q} \right) \frac{\vec{r}_{ji}}{r_{ij}} \right], \quad i \neq j \quad (5)$$

where m_i and \vec{r}_{ji} are mass of P_i and the vector from P_j to P_i ; K is the total number of ambient particles interacting with particle i . In the present study, only the nearest neighboring particles are considered which is addressed by Wang and Ostoja-Starzewski [4].

The derivation of four parameters in Eq. (1) from MD structures is conducted on a cubic body [4]. A face-centered cubic (*f.c.c*) lattice for both atomic and quasi-particle structures is chosen. If p , q and r_0 are given, then, by conditions of mass and energy conservation, G and H

can be derived. Consequently, Young's modulus is evaluated by Eq. (2) and tensile strength by Eq. (4). To represent an expected material property, we would have to do many sets of testing until a unique (p, q) is found to match both Young's modulus and tensile strength of the material. The complete derivation process is described below.

First, for the atomic structure (MD model), we have:

$$\text{interaction potential energy (ergs): } \phi_a = \left(\frac{G_a r^{1-p_a}}{1-p_a} + \frac{H_a r^{1-q_a}}{1-q_a} \right) \times 10^{-8} \quad (6)$$

Young's modulus (*GPa*) is obtained from Eq. (2) and tensile strength (*MPa*) from Eq. (4).

Total number of atoms in $A \times B \times C$ cubic material body:

$$N^* = \left(\frac{A \times 10^8}{r_a} + 1 \right) \times \left(\frac{B \times 10^8}{r_a \sin 60^\circ} + 1 \right) \times \left(\frac{C \times 10^8}{r_a \sqrt{6}/3} + 1 \right) \quad (7)$$

In Eqs. (6) and (7), r_a is equilibrium position of the simulated material in atomic structure, and p_a , q_a are the exponential parameters in atomic structure. Note that, for a Lennard-Jones interaction case, $p_a = 7$ and $q_a = 13$.

Next, for the quasi-particle structure (PM model), we have interaction force (*dynes*) as in Eq. (1).

Interaction potential energy (*ergs*):

$$\phi = \frac{G r^{1-p}}{1-p} + \frac{H r^{1-q}}{1-q}, \text{ for } p > 1; \quad \phi = G \ln r + \frac{H r^{1-q}}{1-q}, \text{ for } p = 1 \quad (8)$$

$$\text{total number of quasi-particles in PM system: } N = i_{\max} \times j_{\max} \times k_{\max} \quad (9)$$

We now postulate the equivalence of MD and PM models. From the mass conservation, we calculate the mass of each quasi-particle m based on atomic mass m_a :

$$m = N^* \times m_a / N \quad (10)$$

$$\text{From the energy conservation, we have: } (N \times \phi)_{r=r_0} = (N^* \times \phi_a)_{r=r_a} \quad (11)$$

$$\text{under the requirement: } F(r_0) = 0 \quad (12)$$

From equations (11), (12), we now derive Young's modulus E :

for $p = 1$:

$$G = Hr_o^{1-q}, \quad H = \frac{(N^* \times \phi_a)_{r=r_a} (1-q)}{N(1-q)r_0^{1-q} \ln r_0 - r_0^{1-q}}, \quad E = -Gr_0^{-3} + qHr_0^{-q-2} \quad (13)$$

for $p > 1$:

$$G = Hr_o^{1-q}, \quad H = \frac{(N^* \times \phi_a)_{r=r_a} (1-p)(1-q)}{N(p-q)} r_0^{q-1}, \quad E = -pGr_0^{-p-2} + qHr_0^{-q-2} \quad (14)$$

Similarly, tensile strength can be obtained under $dF(r_a)/dr = 0$. Evidently, the four parameters (p, q) , r_0 and V affect E and σ_{TS} .

We have established the equations for G, H, p and q , and carried out a parametric study to find the differing effects on p, q, V and r_0 [4]. Herein, we summarize the obtained rules as follows:

- (i) The larger the values of (p, q) are adopted, the larger is E generated. This is typically associated with the material becoming more brittle than ductile, albeit there is a range of toughness to choose from. Also, with E going up, there is a fragmentation into a larger number of pieces.

- (ii) In the case of $p = 1$, the larger r_0 spacing is adopted, the higher is Young's modulus of the PM material. On the contrary, in the special case of $p \neq 1$, there is an opposite trend. In any case, this increase or decrease does not change very much.
- (iii) In the case of $p \neq 1$, while keeping the volume fixed, an increase of r_0 produces a decrease of Young's modulus. The situation is again opposite in the case of $p = 1$.
- (iv) A uniform augmentation of volume V by dilation in all three coordinate directions (xyz), at any (p, q) combination, results in Young's modulus increasing first strongly and then leveling off.

For elastic-brittle materials, a general format of linear dynamical equation is often employed for axial springs [13],

$$F = \begin{cases} -S_0(r - r_0) & \text{for } r_c \leq r \leq r_t \\ 0 & \text{otherwise} \end{cases} \quad (15)$$

with r being the distance between two particles. Following the derivation rules in lattice models addressed in [13], we get the axial stiffness for 1D and 2D structure are $S_0 = E \bullet r_0 / 2$ and $E \bullet r_0$, respectively. E the Young modulus and r_0 the equilibrium spacing between the contiguous particles.

In Equation (14), r_c and r_t are the fracture positions applied for compression and tension, respectively, which in practice need to be empirically determined.

An analogous angular spring interaction scheme to Eq. (14) yields,

$$F_\beta = \begin{cases} -S_\varphi(\varphi - \varphi_0) & \text{for } \varphi_c \leq \varphi \leq \varphi_t \\ 0 & \text{otherwise} \end{cases} \quad (16)$$

with φ_0 the equilibrium angle between adjacent particles, and φ the angular displacement. φ_c and φ_t in Eq. (16) are the angular fracture coefficients applied for compression and tension, respectively, which are also needed to be determined by empirical tests.

The 2D angular stiffness S_ϕ in Eq. (16) is after Wang, *et al.* [9],

$$S_\phi = \frac{\sqrt{3}(1-3\nu)Er_0^2}{18(1-\nu^2)} \quad (17)$$

with ν the Poisson's ratio.

The leapfrog method, with second-order accuracy, is employed in the HLPM simulations. The leapfrog formulas relating position, velocity and acceleration for particles P_i ($i = 1, 2, \dots, N$) [16] are

$$\vec{V}_{i,1/2} = \vec{V}_{i,0} + \frac{(\Delta t)}{2} \vec{a}_{i,0} \quad (\text{starter formula}) \quad (18)$$

$$\vec{V}_{i,k+1/2} = \vec{V}_{i,k-1/2} + (\Delta t) \vec{a}_{i,k}, \quad k = 1, 2, 3, \dots \quad (19)$$

$$\vec{r}_{i,k+1} = \vec{r}_{i,k} + (\Delta t) \vec{V}_{i,k+1/2}, \quad k = 0, 1, 2, \dots \quad (20)$$

where $\vec{V}_{i,k}$, $\vec{a}_{i,k}$ and $\vec{r}_{i,k}$ are the velocity, acceleration and position vectors of particle i at time $t_k = k\Delta t$, Δt is the time step. $\vec{V}_{i,k+1/2}$ stands for the velocity of particle i at time $t_k = (k + 1/2)\Delta t$, and so on. Notably, the leapfrog method is of second-order accuracy: $O((\Delta t)^2)$.

The safe time step is after the derivation result by Hockney & Eastwood [16]:

$$\Omega \Delta t \ll 2, \quad \Omega = \left(\frac{1}{m} \left| \frac{dF}{dr} \right|_{\max} \right)^{1/2} \quad (21)$$

It is noted that the discretized scheme and deterministic time increment of HLPM as shown by Eqs. (18-21) is completely identical to what is used by PFC [3] and PFEM [7].

To readily describe the breakage effect on material, we define a concept of fracture density [5]. By this definition, the local fracture density of particle i , $f_{i_{den.}}$, is equal to the ratio of its current number of broken bonds, N_{b_i} to its original number of bonds, N_{o_i} , i.e.,

$$f_{i_{den.}} = \frac{N_{b_i}}{N_{o_i}} \quad (22)$$

It is clearly seen that a big $f_{i_{den.}}$ value indicates a severe failure locally occurring at i .

Note that different failure criterion for inelastic and elastic materials shown in Eq. (1) and (15) are employed as a cut-off for the axial interaction force. For instance, necking position, $dF(r_d)/dr = 0$, is adopted for inelastic material expressed in Eq. (1); for elastic-brittle material expressed in Eq. (15), using tensile stress, σ_{TS} , from Hooke's law, we determine the failure strain ε_{max}

$$\frac{r_{max} - r_0}{r_0} = \varepsilon_{max} = \frac{\sigma_{TS}}{E} \quad (23)$$

and the displacement threshold for fracture to occur, r_{max} .

Angular failure criterion follows the analogous scheme to Eq. (22) whereas shear strength is accounted for.

3. Results

3.1 HLPM prediction of wave propagation in 1D and 2D elastic-brittle material

In this section we report a preliminary HLPM study of wave propagation in a 1D and 2D elastic-brittle bar, subjected to dynamic and kinematic loading, respectively. The computational domain for 1D and 2D are $L = 12.7\text{ cm}$ in length (one layer of particles) and $12.7\text{ cm} \times 1.27\text{ cm}$ (fifteen layers of particles), respectively, with an initial particle spacing

$r_0 = 0.1 \text{ cm}$; two points are selected at $L/4$ and $L/2$ away from the left end for calculating the wave propagation speed. Dynamic and kinematic conditions are, respectively, applied to the left end at 97.8 MPa and constantly 60.0 m/s ; the right end is fixed and the remaining boundaries are traction free, shown in Fig. 2(a, b). The material parameters are: Young's modulus $E = 3.0 \text{ GPa}$, density $\rho = 1140 \text{ kg/m}^3$, and failure strain $\varepsilon_{\max} = 0.02$. For a simplicity, we assume the Poisson's ratio of the material equal to $1/3$. Consequently, the angular spring effect is absent [9], and only axial interaction is accounted for and determined after Eq. (15).

The classical wave theory gives that the wave propagation speeds in the above-mentioned 1D and 2D material bars are, respectively [17],

$$1\text{D}: C_{p(1D)} = \sqrt{E/\rho} \approx 1622.0 \text{ m/s} \quad (24)$$

$$2\text{D}: C_{p(2D)} = \sqrt{(K + 4G/3)/\rho} \approx 1986.0 \text{ m/s} \quad (25)$$

In Eq. (25) K and G are the bulk and shear modulus, respectively.

3.1.1 Dynamic boundary condition

A dynamic boundary condition with 97.8 MPa is applied to the left end of 1D and 2D bar, respectively. Figure 3 displays the HLPm results of the horizontal displacement for 1D and 2D at $X = L/2$. From Figure 3(a) it is seen that the wave propagation profiles for 1D and 2D are different due to the existing difference of wave propagation speed in 1D from 2D structure; however, the individual profile is analogous to the Hopkinson bar test [1]. Via Figure 3(b), we can calculate that the horizontal wave speed values travelling in the 1D and 2D bar are equal to 1455.0 m/s and 2133.0 m/s , respectively. These results indicate that, the 1D simulation result is smaller than the analytical solution, 1622.0 m/s , while the 2D result is bigger than the analytical value, 1986.0 m/s . The reason for the existing discrepancies is not very clear. It may arise from the difference of wave propagation in lattice/particle structure from that of the continuum media.

However, we can still conclude that HLPM is able to correctly capture the wave propagation of solids.

Figure 4 displays the HLPM results of the vertical displacement for the 1D and 2D cases at $X = L/2$. It is seen that an oscillation is emergent for the 2D simulation due to the reflection of wave from the lateral boundaries.

3.1.2 Kinematic boundary condition

A kinematic boundary condition with 60.0 cm/s is constantly applied to the left end of the 1D and 2D bar, respectively. Figure 5 displays the HLPM results of the horizontal displacement for the 1D and 2D simulations at $X = L/2$. From Figure 5(a) it is seen that the wave propagation profiles for both of the 1D and 2D cases are equally increased in amplitude after each period of wave reflection; this coincides with the knowledge of wave propagation with a constant load condition. Via Figure 5(b), we can calculate that the horizontal wave speed value for 1D and 2D cases are equal to 1455.0 m/s and 2133.0 m/s , respectively. These values are identical to the above-shown 1D and 2D cases subject to dynamic loading.

Figure 6 displays the HLPM results of the vertical displacement for 1D and 2D at $X = L/2$. Compared with the dynamic loading case in Figure 4, it is seen that the vertical amplitude is smaller for employing a kinematic loading than a dynamic loading.

3.1.3 HLPM of wave propagation with various loadings

Within an elastic extent, wave speed should be identical and independent of the loading change. Therefore, next, we will employ different loading rates to the above-mentioned cases to test the reliability of HPLM.

We completely adopt the same geometry as what we have used for the above-mentioned 1D and 2D studies except that different dynamic and kinematic loading values are applied, respectively. Since the vertical effects are trivial, only the horizontal results are shown in the following.

For the dynamic loading test, 48.9 *MPa* is in addition applied to the left end of 1D and 2D bar, respectively. Figure 7 illustrates the HPLM comparisons of horizontal displacement for 1D and 2D bar, respectively, recorded at $X = L/2$, in which dynamic boundary conditions, 48.9 *MPa* and 97.8 *MPa*, are applied.

For the kinematic loading test, 50.0 *cm/s* is in addition applied to the left end of 1D and 2D bar, respectively. Figure 8 illustrates the HPLM comparisons of horizontal displacement for 1D and 2D bar, respectively, recorded at $X = L/2$, in which kinematic boundary conditions, 50.0 *cm/s* and 60.0 *cm/s* are applied.

From Figure 7 and 8, we clearly see that, for 1D and 2D simulations, either dynamic or kinematic loading is employed, the amplitude is different associated with the loading rate change, while the wave propagation speed is independent of this change. Therefore, we conclude that HPLM is reliable in the wave prediction.

3.2 HPLM study of wave induced fracture - spall crack formation

Spall crack formation is the direct consequence that arises from wave interaction in solids - tension and compression wave interactions; the area, where the tension and compression wave meet, is highly stretched, and a spall crack consequently occurs.

In the following, spall crack formations due to high speed impact and blasting load are preliminarily simulated, respectively.

3.2.1 Spall crack formation due to high speed impact

The dimension of the target is set as $5.2\text{cm} \times 0.68\text{cm}$ while the two different sizes of the impactor are set as $5.2\text{cm} \times 0.20\text{cm}$ and $2.6\text{cm} \times 0.20\text{cm}$, respectively. The material properties of both impactor and target are set to be identical, in which we have the Young's modulus $E = 163.24\text{ GPa}$, the tensile strength $\sigma_{TS} = 478.25\text{ MPa}$, failure strain $\varepsilon_{\max} = 0.10$, and density

$\rho = 8900.0 \text{ kg/m}^3$. The impactor's initial dropping speed is 260 m/s . Traction free boundary conditions are applied to all the boundaries.

Figure 9 shows the qualitative comparison of spall crack formation of HPLM simulations with the results from the analogous molecular dynamic (MD) simulations by Krivtsov [18, 19]. As seen from Figure 9(b), the spall crack formation is clearly captured by HLPM. We see that the tension wave, the wave reflected from the bottom of the target, meets the compression wave, the wave reflected from the top of the impactor, at a thin layered area with a distance away from the bottom of the target. The two kinds of wave propagate in different directions alongside the Y-axis when they meet; this leads to a high stretching to the material herein, thus a spall crack zone is generated. It is also discovered that the length of spall crack formation is smaller than that of the impactor.

Next, the above-mentioned target coated with a high strength layer at the bottom of the target, but with different coating strength at the coating interface, is investigated to find out the protective effect of spallation.

We choose the coating layer with the same density as that of the above-mentioned impactor and target, but with more stronger material strength properties, i.e., the Young's modulus $E = 380.89 \text{ GPa}$, the tensile strength $\sigma_{TS} = 841.97 \text{ MPa}$ and failure strain $\varepsilon_{\max} = 0.07$. Meanwhile, two coating schemes at the interface are attempted with strong and weak coating strength, respectively. A strong coating at the interface is with the same strength parameters as used for the impactor/target; while a weak coating with the Young's modulus $E = 16.74 \text{ GPa}$, the tensile strength $\sigma_{TS} = 93.37 \text{ MPa}$ and failure strain $\varepsilon_{\max} = 0.29$. The initial impact speed of the impactor is still 260 m/s .

Figure 10(a, b) shows the HLPM simulations of employing weak and strong coating strengths at the interface, respectively. In general, we see that, in our cases, even a high strength retrofitting material is coated at the target, spall crack formation is not prevent. This implies that prevention of material from spallation under extreme loadings is difficult; it needs the coating material with super strength. Thus, the research is worth advancing. From Figure 10, we also see

that, for a weak coating, the spall cracks occur not only inside the target, but also at the coating interface and inside the retrofitting material, whereas for a strong coating, the spall cracks only form inside the target.

3.2.1 Spall crack formation due to blasting

Preliminary HPLM simulations of spall crack formation with different spatial blasting load sources are presented in the following.

Figure 11(a, b) shows HPLM simulation of spall crack formation during a blasting process with the detonation installed in one rectangular cavity. All the outer boundaries are traction free. The blasting wave trajectory in the material body is clearly captured as marked by an arrow in Figure 11(a). Figure 11(b) displays the final fracture pattern; it is found that the spall cracks are mainly formed in the areas adjacent to the lateral boundaries.

Figure 12(a, b) shows the HPLM of spall crack formation during a blasting process with detonation installed in two circular cavities located in parallel and diagonally, respectively. Figure 12(a) indicates that explosive from two cavities set in parallel causes more severe spall crack formation horizontally, and the fragments are generated within the extent of circular diameter on the two vertical outer boundaries. Figure 12(b) displays that explosive from two cavities set diagonally causes more severe spall crack formation diagonally on the lateral outer boundaries. This failure formation coincides with the direction of the explosive source setting.

The spall crack formation in pattern and extent arises from the complicated tension/compression wave interactions in materials. Wherever the tension/compression waves meet, the material herein is highly stretched, and, thus, fracture or fragmentation is formed. Via the simulations, the fracturing efficiency associated with the spatial explosive source setup is exhibited. The underway research will benefit the explosive fracturing applications.

4. Concluding remarks

In this paper, a hybrid lattice particle modeling (HPLM) method is first employed for a study of wave propagation in 1D and 2D material bar, and the results are verified with the

analytical solutions. Next, the HLPM is applied to the simulation of wave propagation induced fracture, spall cracks, due to impact and blasting. In the impact case, a functionally designed infrastructure material coated with a high strength layer, but with different coating strengths at the interface, is also investigated to find out the protective effect of spallation.. Via this study, the following benefits are obtained.

From the serial analyses of the preliminary simulation results obtained by using HLPM, we obtain several important conclusions:

- (1) No need for remeshing. Re-meshing is known as an overwhelming challenge for FEM whereas HLPM does not bother it at all. In HLPM, fracture is created when a bond (spring) is broken by translational force. This provides HLPM a unique power to be able to quite easily overcome a “discontinuity of material” problem.
- (2) No stress intensity required. In HLPM, a bond (spring) is broken and fracture is thus resulted wherever the critical failure strain reaches.
- (3) HLPM can correctly capture wave propagation of solids. From the HLPM applications of wave propagation induced fracture problems, spall cracks, due to impact and blasting, we conclude that HLPM can successfully capture spall crack formation subject to impact and blasting, respectively. In the impact case, a functionally designed infrastructure material coated with a high strength layer, but with different coating strengths at the interface, is also investigated to find out the protective effect of spallation. The modeling results demonstrate that prevention of material from spallation under extreme loadings is difficult; it needs the coating material with super strength. In the blasting study, the fracturing efficiency associated with the explosive setup is investigated. This will benefit the explosive fracturing applications.

In summary, the outcomes of this paper can provide important lessons for fracture control which has remarkable significance to engineering applications. Of course, more modeling validations and improvement work are required. The ultimate application for HLPM is aimed at shock synthesis.

Acknowledgement

This work was partially supported by the funding received under a subcontract from the Department of Homeland Security-sponsored Southeast Region Research Initiative (SERRI) at the Department of Energy's Oak Ridge National Laboratory, USA. Authors wish to acknowledge the partial support for this research by ONR Grant# N00014-07-1-1010, Office of Naval Research, Solid Mechanics Program (Dr. Yapa D.S. Rajapakse, Program Manager).

References

- [1] Kaiser, M. A., 1998. Advancements in the split Hopkinson bar test. *Master Thesis*, Virginia Polytechnic Institute.
- [2] Monaghan, J., 2005. Smoothed particle hydrodynamics, *Rep. Prog. Phys.*, **68**(1), 1703-1759.
- [3] Cundall, P.A., 1988. Computer simulations of dense sphere assemblies, *Micromechanics of Granular Materials*, 113-123.
- [4] Wang, G., Ostoja-Starzewski, M., 2005. Particle modeling of dynamic fragmentation – I: theoretical considerations, *Computational Materials Science*, **33**, 429-442.
- [5] Wang, G., Radziszewski, P. and Ouellet, J., 2008. Particle modeling simulation of thermal effects on ore breakage, *Computational Materials Science*, **43**, 892-901.
- [6] Quan, X., Birnbaum, N.K., Cowler, M.S., Gerber, B.I., Clegg, R.A. and Hayhurst, C.J., 2003. Numerical simulation of structural deformation under shock and impact loads using a coupled multi-solver approach, *5th Asia-Pacific Conference on Shock and Impact Loads on Structures*, November 12-14, Hunan, China.
- [7] Oñate, E., Idelsohn, S.R., Pin, F. D, and Aubry., R., 2004. The particle finite element method. An Overview, *International Journal Computational Method*, **1**(2), 267-307.
- [8] Chen, Z. and Brannon, R., 2002. An evaluation of the material point method, Sand Report, Sandia National Laboratories.
- [9] Wang, G., Al-Ostaz, A., Cheng, A.H.-D. and Mantena, P.R., 2009. Hybrid Lattice Particle Modeling: Theoretical Considerations for a 2-D Elastic Spring Network for Dynamic Fracture Simulations, *Computational Materials Science*, **44**, 1126-1134.
- [10] Ostoja-Starzewski, M., 2002. Lattice models in micromechanics, *Appl. Mech. Rev.*, **55**(1), 35-60.

- [11] Ostoja-Starzewski, M., 2007. *Microstructural Randomness and Scaling in Mechanics of Materials*, in Modern Mechanics and Mathematics Series, Chapman & Hall/CRC/Taylor & Francis.
- [12] Ostoja-Starzewski, M., Wang, G., 2006. Particle Modeling of Random Crack Patterns in Epoxy Plates, *Probabilistic Engineering Mechanics*, **21**, 267-275
- [13] Wang, G., Al-Ostaz, A., Cheng, A.H.-D. and Mantena, P.R., 2008. Particle modeling of a polymeric material (nylon-6, 6) due to the impact of a rigid indenter, *Computational Materials Science*, **44**, 449-463.
- [14] Wang, G., 2009. Particle modeling of polymeric material indentation study, *Eng. Fract. Mech.*, **76**, 1386-1395.
- [15] Ashby, M.F., Jones, D.R.H., 1980. *Engineering Materials 1: An Introduction to Their Properties and Applications*, Pergamon Press.
- [16] Hockney, R.W., Eastwood, J.W., 1999. *Computer Simulation Using Particles*, Institute of Physics Publishing.
- [17] Meyers, M.A., 1994. *Dynamic behavior of materials*, A Wiley-interscience Publication.
- [18] Krivtsov, A. M., 1999. Relation between spall strength and mesoparticle velocity dispersion, *International Journal of Impact Engineering*, **23**, 477-487.
- [19] Krivtsov, A. M., 1999. Computer simulation of spall crack formation, *Structural Dynamics – EURO DYN '99*, Fryba & Nařrstek (eds) c 1999 Balkema, Rotterdam, **ISBN 90 5809 056 6**, 475-477.

Figures

Figure 1 A material impact simulation by using FEM employing Arbitrary Lagrange Euler (ALE) re-meshing technique, and smoothed particle hydrodynamics (SPH) [5].

Figure 2 Schematic of computational domain setup for (a) 1D and (b) 2D. Particle spacing $r_0 = 0.2 \text{ cm}$.

Figure 3 HPLM prediction of horizontal displacement for 1D and 2D bar, respectively. (a) horizontal displacement recorded at $X = L/2$; (b) horizontal displacement recorded at $X = L/4$ and $X = L/2$. Dynamic boundary condition is applied.

Figure 4 HPLM prediction of vertical displacement recorded at $X = L/2$ for 1D and 2D bar, respectively. Dynamic boundary condition is applied.

Figure 5 HPLM prediction of horizontal displacement for 1D and 2D bar, respectively. (a) horizontal displacement recorded at $X = L/2$; (b) horizontal displacement recorded at $X = L/4$ and $X = L/2$. Kinematic boundary condition is applied.

Figure 6 HPLM prediction of vertical displacement recorded at $X = L/2$ for 1D and 2D bar, respectively. Kinematic boundary condition is applied.

Figure 7 HPLM prediction of horizontal displacement for 1D and 2D bar, respectively, recorded at $X = L/2$. (a) 1D; (b) 2D. Dynamic boundary conditions, 48.9 MPa and 97.8 MPa are applied.

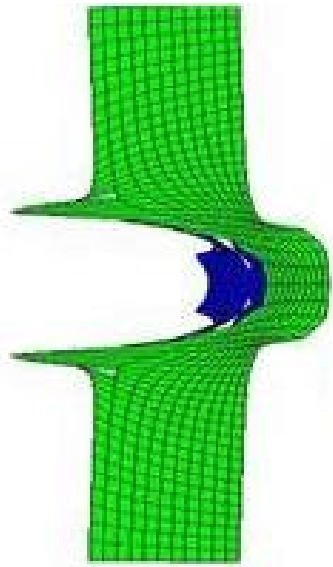
Figure 8 HPLM prediction of horizontal displacement for 1D and 2D bar, respectively, recorded at $X = L/2$. (a) 1D; (b) 2D. Kinematic boundary conditions, 50.0 cm/s and 60.0 cm/s are applied.

Figure 9 Qualitative comparison of spall crack formation of HPLM with MD. (a) MD simulations, (b) HPLM simulations. Impact speed = 260.0 m/s

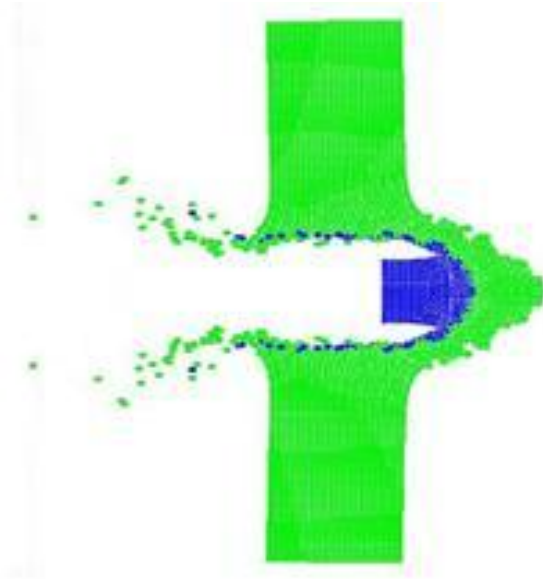
Figure 10 HPLM of spall crack formation with bottom layer coating by (a) ductile material, and (b) rigid material.

Figure 11 HPLM of spall crack formation during a blasting process with detonation installed from one cavity. (a) blasting wave propagation; (b) final spall crack formation.

Figure 12 HPLM of spall crack formation during a blasting process with detonation installed from two cavities. (a) detonation from two cavities located in parallel; (b) detonation from two cavities located diagonally.

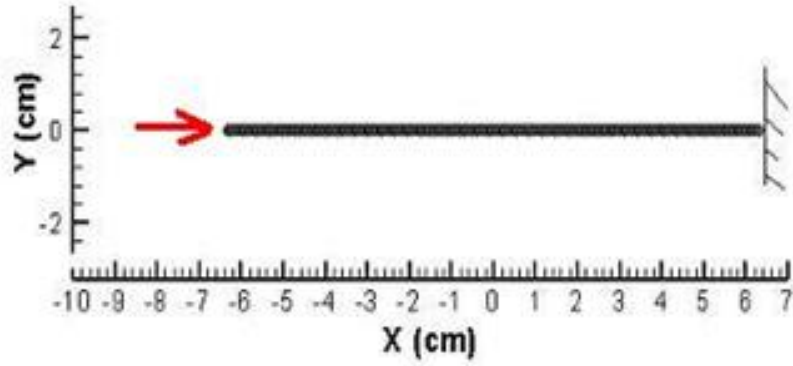


(a) ALE

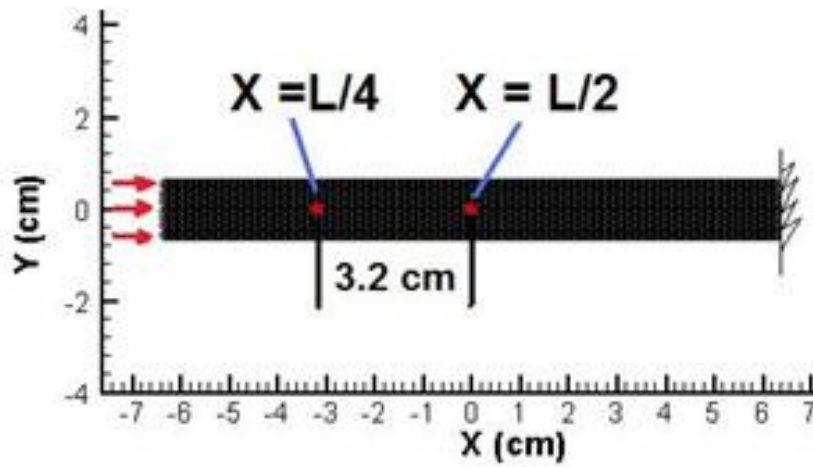


(b) SPH

Figure 1 A material impact simulation by using FEM employing Arbitrary Lagrange Euler (ALE) re-meshing technique, and smoothed particle hydrodynamics (SPH) [6].

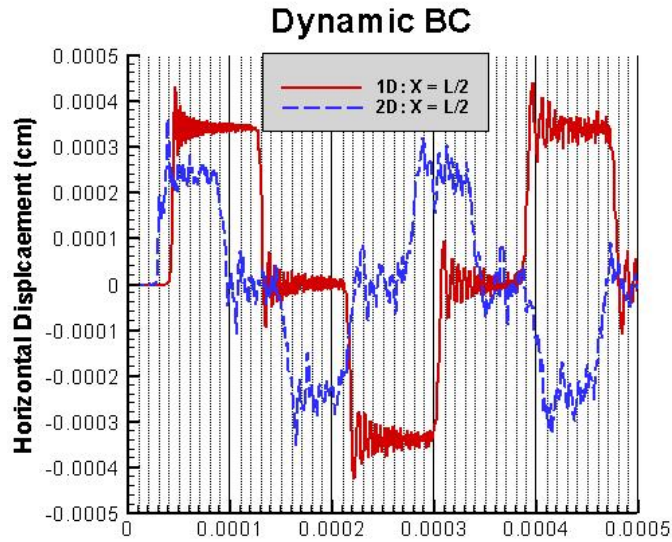


(a) 1D

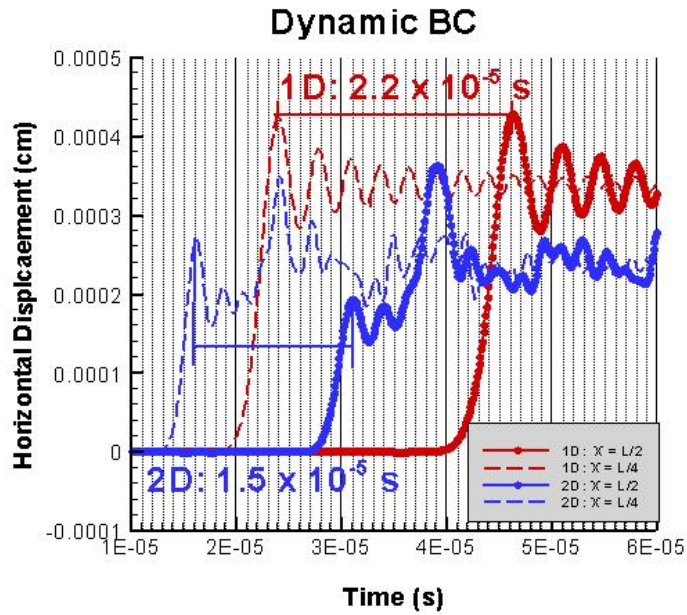


(b) 2D

Figure 2 Schematic of computational domain setup for (a) 1D and (b) 2D. Particle spacing $r_0 = 0.2 \text{ cm}$.



(a) horizontal displacement recorded at $X = L/2$.



(b) horizontal displacement recorded at $X = L/4$ and $X = L/2$.

Figure 3 HPLM prediction of horizontal displacement for 1D and 2D bar, respectively. (a) horizontal displacement recorded at $X = L/2$; (b) horizontal displacement recorded at $X = L/4$ and $X = L/2$. Dynamic boundary condition is applied.

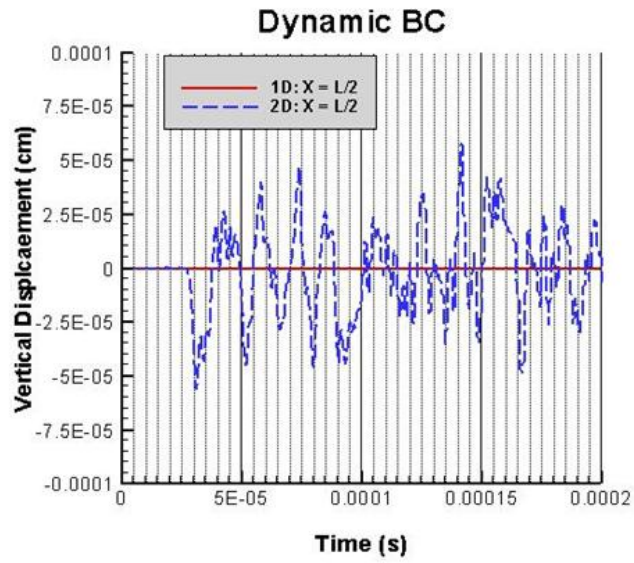
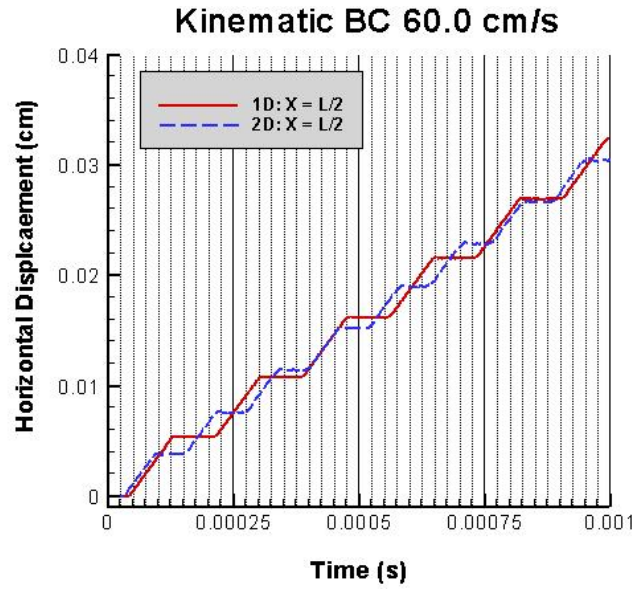
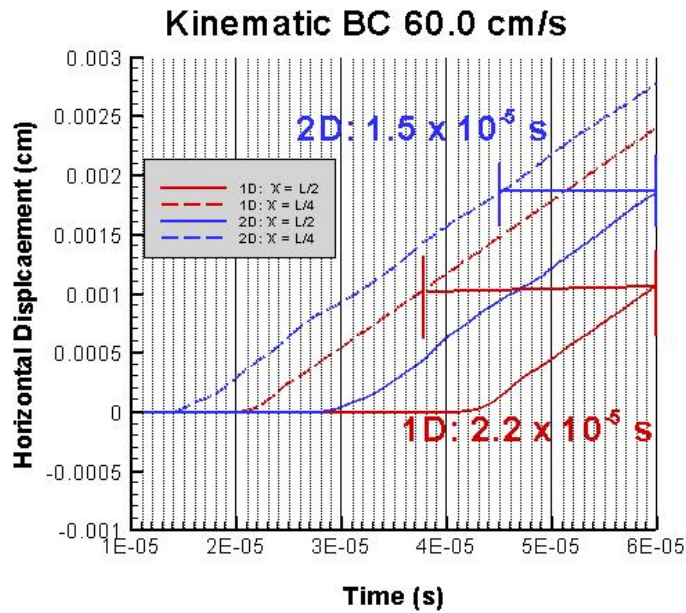


Figure 4 HPLM prediction of vertical displacement recorded at $X = L/2$ for 1D and 2D bar, respectively. Dynamic boundary condition is applied.



(a) horizontal displacement recorded at $X = L/2$.



(b) horizontal displacement recorded at $X = L/4$ and $X = L/2$.

Figure 5 HPLM prediction of horizontal displacement for 1D and 2D bar, respectively. (a) horizontal displacement recorded at $X = L/2$; (b) horizontal displacement recorded at $X = L/4$ and $X = L/2$. Kinematic boundary condition is applied.

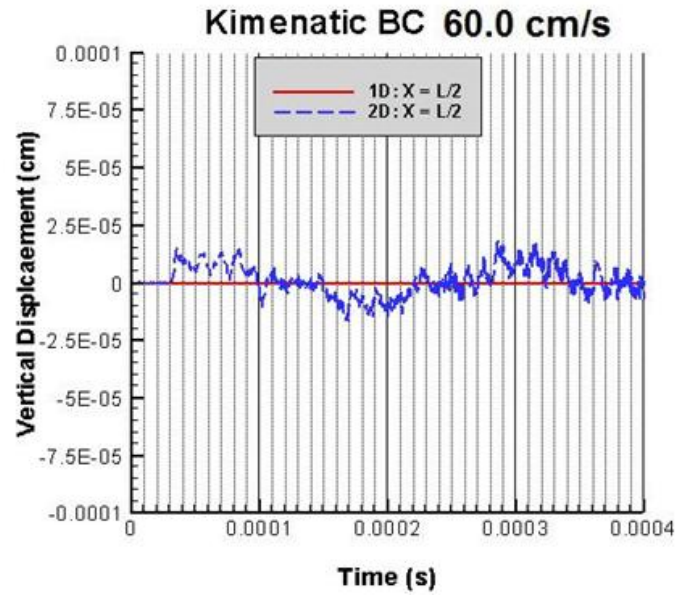
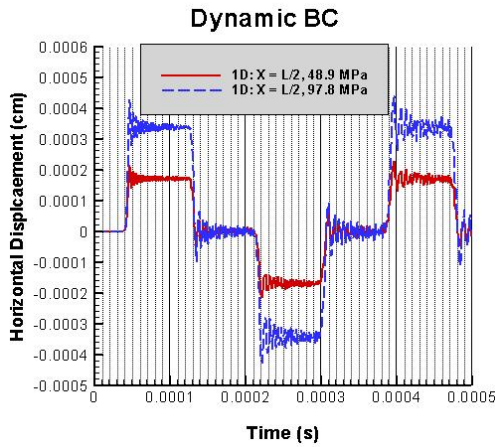
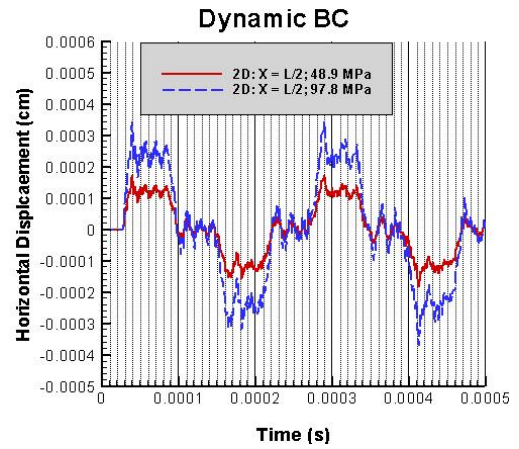


Figure 6 HPLM prediction of vertical displacement recorded at $X = L/2$ for 1D and 2D bar, respectively. Kinematic boundary condition is applied.

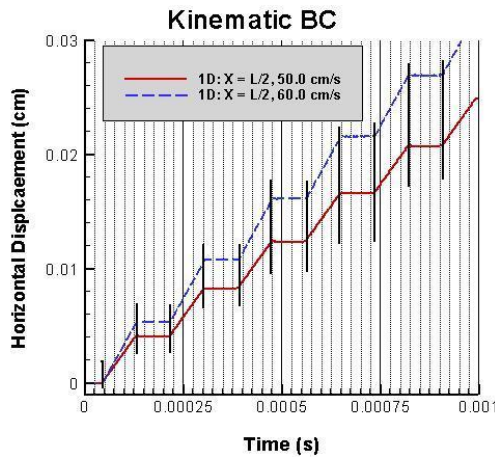


(a) 1D

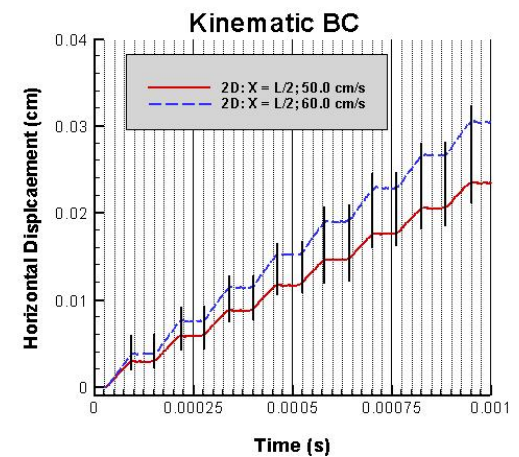


(b) 2D

Figure 7 HPLM prediction of horizontal displacement for 1D and 2D bar, respectively, recorded at $X = L/2$. (a) 1D; (b) 2D. Dynamic boundary conditions, 48.9 MPa and 97.8 MPa are applied.



(a) 1D

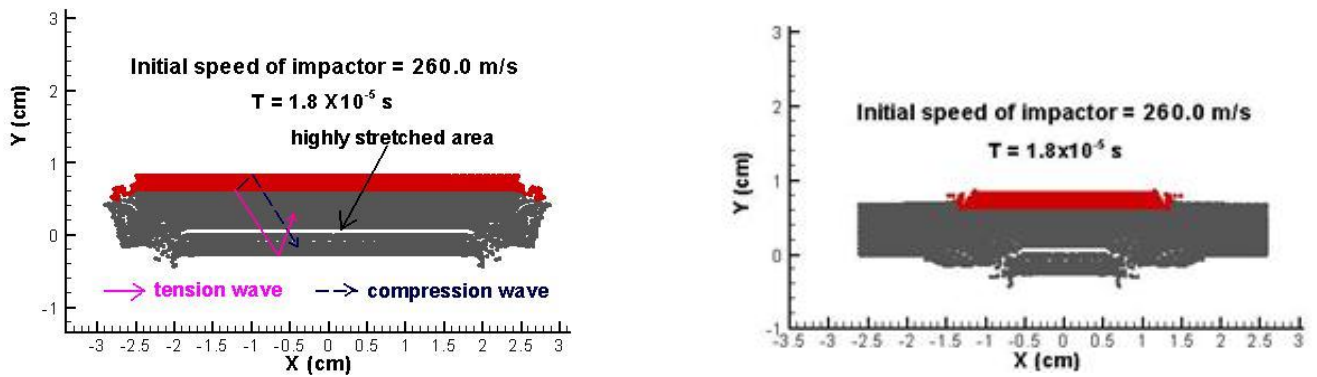


(b) 2D

Figure 8 HPLM prediction of horizontal displacement for 1D and 2D bar, respectively, recorded at $X = L/2$. (a) 1D; (b) 2D. Kinematic boundary conditions, 50.0 cm/s and 60.0 cm/s are applied.

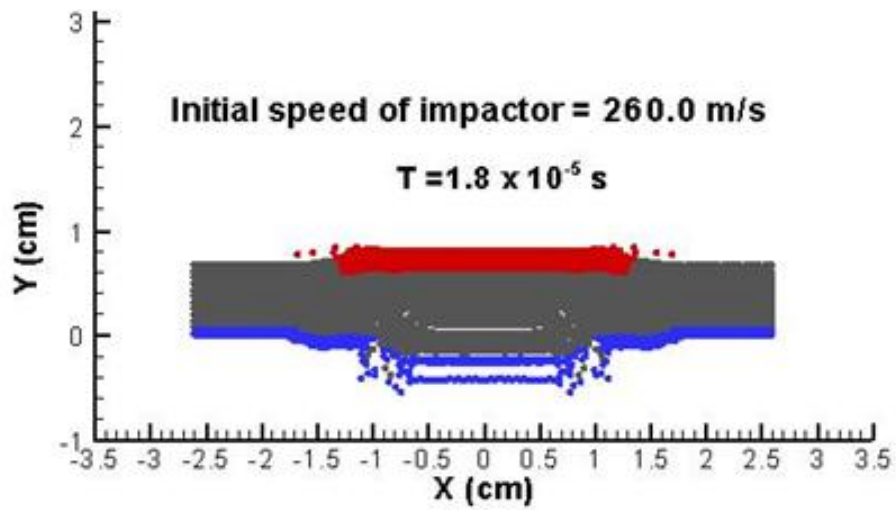


(a) MD simulations [17, 18]

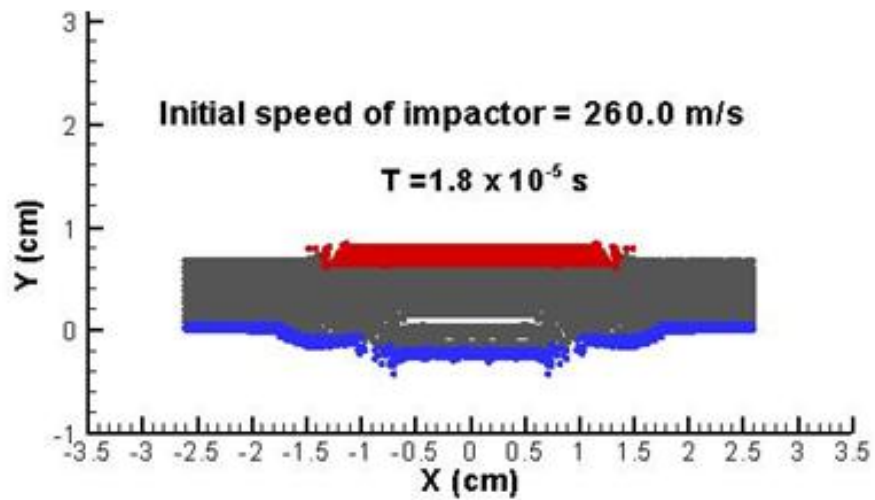


(b) HPLM simulations

Figure 9 Qualitative comparison of spall crack formation of HPLM with MD. (a) MD simulations, (b) HPLM simulations. Impact speed = 260.0 m/s.

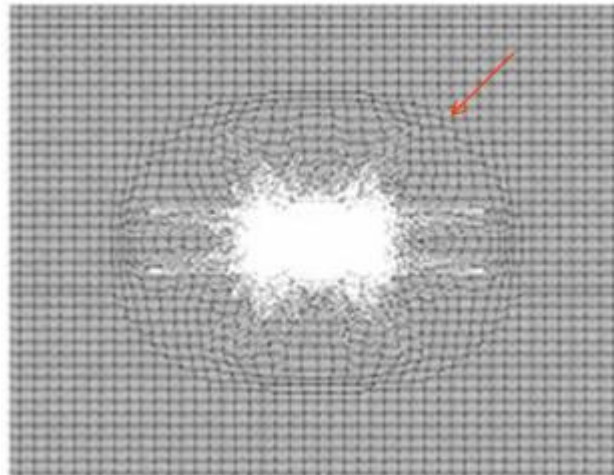


(a) ductile coating.

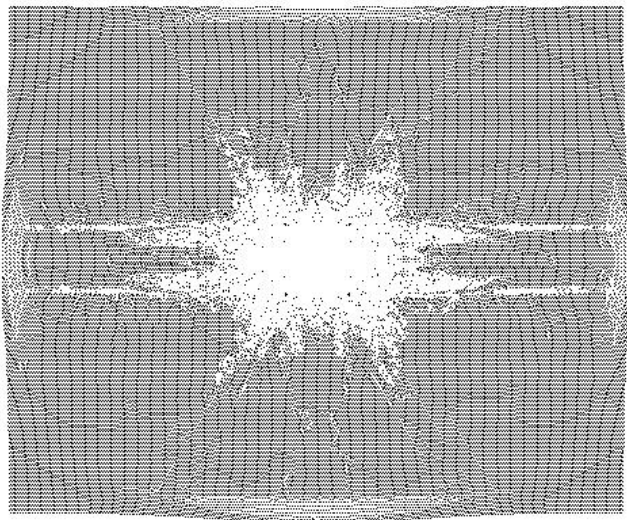


(b) rigid coating.

Figure 10 HPLM of spall crack formation with bottom layer coating by (a) ductile material, and (b) rigid material.

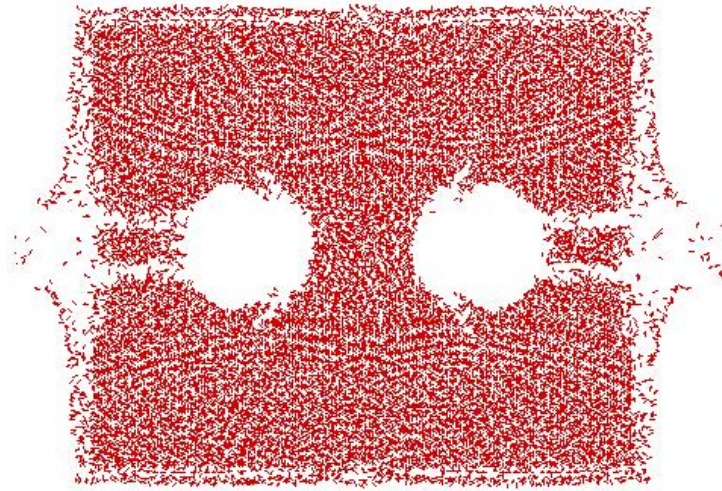


(a) blasting wave propagation.

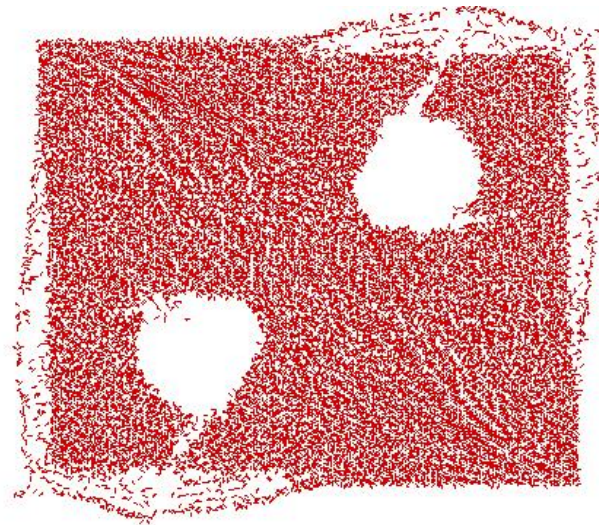


(b) final spall crack formation.

Figure 11 HPLM of spall crack formation during a blasting process with detonation installed from one cavity. (a) blasting wave propagation; (b) final spall crack formation.



(a) detonation from two cavities located in parallel.



(b) detonation from two cavities located diagonally.

Figure 12 HPLM of spall crack formation during a blasting process with detonation installed from two cavities. (a) detonation from two cavities located in parallel; (b) detonation from two cavities located diagonally.